Higher-dimensional Fermiology in bulk moiré metals

https://doi.org/10.1038/s41586-026-10173-8

Received: 18 September 2025

Accepted: 22 January 2026

Kevin P. Nuckolls[1,7], Nisarga Paul[1,7], Alan Chen[2], Filippo Gaggioli[1], Joshua P. Wakefield[1], Avi Auslender[3,4], Jules Gardener[3], Austin J. Akey[3], David Graf[5], Takehito Suzuki[6], David C. Bell[3,4], Liang Fu[1] & Joseph G. Checkelsky[1] ✉

In the past decade, moiré materials have revolutionized how we engineer and control quantum phases of matter[1,2]. They are versatile platforms for strongly correlated electronic phenomena[3,4] and support new ferroelectric[5,6], magnetic[7] and superconducting states[8]. Among incommensurate materials[9], moiré materials are aperiodic composite crystals[10,11] whose long-wavelength superlattices enable tunable properties without chemically modifying their layers. So far, nearly all reports of moiré materials have investigated van der Waals heterostructures assembled far from thermodynamic equilibrium ($T < 150$ °C)[1,2]. Here we introduce a conceptually new approach to synthesizing high-mobility moiré materials in thermodynamic equilibrium. We report a new family of foliated superlattice materials $(Sr_6TaS_8)_{1+\delta}(TaS_2)_8$ that are exfoliatable, incommensurate-lattice, van der Waals crystals. Lattice mismatches between alternating layers generate moiré superlattices, analogous to 2D moiré heterobilayer superlattices, which are coherent throughout these crystals and tunable through synthesis conditions without altering their chemical composition. Quantum oscillation measurements map the complex Fermiology of these moiré metals[12–14], showing that the Fermi surface of the structurally simplest moiré metal comprises more than 40 distinct cross-sectional areas. This is naturally understood by proposing that these bulk moiré metals encode electronic properties of higher-dimensional superspace crystals in ways paralleling well-established crystallographic methods for incommensurate lattices[15,16]. More broadly, our work demonstrates a scalable synthesis approach potentially capable of producing large-area moiré materials for electronics applications and evidences a new material design concept for accessing phenomena proposed in higher dimensions[17–21].

Crystalline order is typically the most stable configuration for atoms to form solids, but this is not always the case even within minerals found in nature[22]. Incommensurate lattice crystals[9], which lack translation symmetry while still supporting long-range order, comprise incommensurately modulated crystals (such as incommensurate ferroelectrics[23]), aperiodic composite crystals (such as misfit layer compounds[24]) and quasicrystals (such as icosahedral intermetallics[25–27]). Atomically incommensurate materials (the last two subclasses) evade the constraints of highly symmetric lattices found in periodic crystals. Furthermore, their electronic properties are difficult to capture using conventional band theory[28–30] because they lack a well-defined Brillouin zone and a real-space unit cell under the physical dimensions of the crystal. Instead, crystallographers describe incommensurate lattices using the mathematical framework of superspace crystals[15,16], emergent higher-dimensional periodic lattices derived from lower-dimensional incommensurate lattices that fully encode their superspace symmetries.

Recently, 2D moiré materials have emerged as a highly tunable class of incommensurate materials[1,2]. 2D moiré materials, like all aperiodic composites, are atomically incommensurate despite having well-defined local atomic coordinations. Like some aperiodic composites, the interference between lattice-mismatched crystalline layers produces a long-wavelength ‘moiré superlattice’ modulation. Notably, moiré superlattices are tunable without altering the chemical composition of their layers (for example, by twisting) and they support new low-energy properties not found in their constituent layers. This includes new band structures and Fermi surfaces[29,30], new interlayer lattice or exchange couplings[5–7] and new correlated and topological phases[3,4].

Here we demonstrate a conceptually new approach to synthesizing high-mobility moiré materials using bulk synthesis techniques, contrasting existing methods that use the low-temperature assembly of mechanically exfoliated van der Waals flakes[1,2]. We report a new family of aperiodic composite crystals, $(Sr_6TaS_8)_{1+\delta}(TaS_2)_8$ for $\delta \approx 0.1$, that emulates the essential properties of lattice-mismatched heterobilayer

[1]Department of Physics, Massachusetts Institute of Technology, Cambridge, MA, USA. [2]Department of Electrical Engineering and Computer Science, Massachusetts Institute of Technology, Cambridge, MA, USA. [3]Center for Nanoscale Systems, Harvard University, Cambridge, MA, USA. [4]Harvard John A. Paulson School of Engineering and Applied Sciences, Harvard University, Cambridge, MA, USA. [5]National High Magnetic Field Laboratory, Tallahassee, FL, USA. [6]Department of Physics, Toho University, Funabashi, Japan. [7]These authors contributed equally: Kevin P. Nuckolls, Nisarga Paul. ✉e-mail: checkelsky@mit.edu

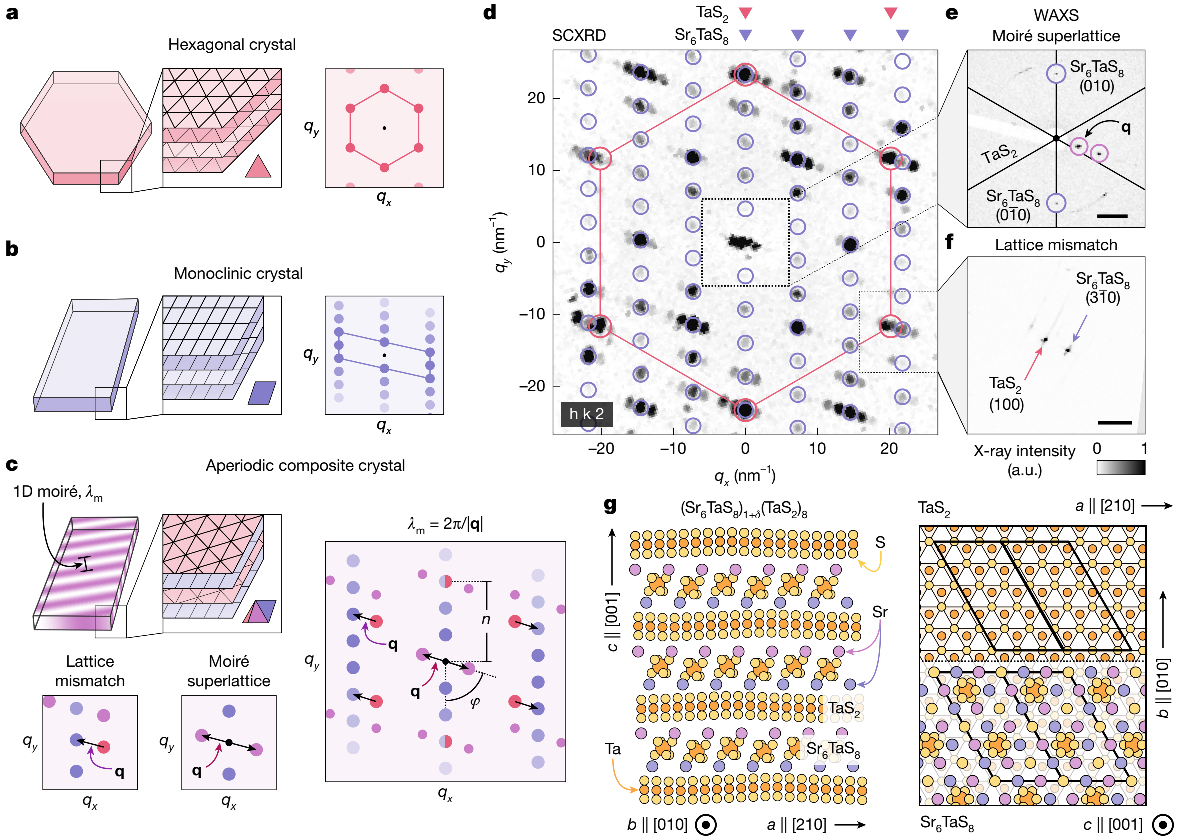

Fig. 1 | Introduction to bulk moiré materials. a, Schematic of a hypothetical hexagonal crystal (left panel) and its expected diffraction pattern (right panel). **b**, Same as **a** but for a monoclinic crystal. **c**, Same as **a** but for a hypothetical aperiodic composite crystal (top-left panel). X-ray and electron diffraction patterns (right panel) show a lattice mismatch of Bragg vectors between neighbouring layers (bottom-left panel) and a long-wavelength moiré superlattice represented by a short **q**-vector (bottom-middle panel). The relevant features of this diffraction pattern can be captured by three quantities: the commensurate Bragg plane order *n*, the moiré wavevector angle φ and the moiré wavevector length $|\mathbf{q}|$. **d**, SCXRD measurement of $(Sr_6TaS_8)_{1+\delta}(TaS_2)_8$, a new aperiodic composite compound. **e**,**f**, Zoomed-in WAXS showing the moiré superlattice and lattice mismatch between the Sr_6TaS_8 and TaS_2 layers. **g**, Proposed highest-symmetry model structure consistent with all structural and stoichiometric characterization measurements. Alternating Sr_6TaS_8 and TaS_2 layers are atomically incommensurate with one another along the *a*-axis and they share commensurate Bragg planes along the *b*-axis. The black parallelogram outline denotes the intralayer unit cell of the Sr_6TaS_8 layer, which is incommensurate with TaS_2 along the *a*-axis. [hkl] crystallographic directions are defined with respect to the TaS_2 lattice. Scale bars, 2 nm^{-1}. a.u., arbitrary units.

moiré materials[1]. Similar to a vertical stack of Sr_6TaS_8/TaS_2 moiré heterobilayers, these are also mechanically exfoliatable van der Waals crystals (Supplementary Information). Therefore, this family is a proof of concept for a potentially scalable approach for producing high-quality moiré materials for next-generation electronics using the tools of solid-state chemistry. $(Sr_6TaS_8)_{1+\delta}(TaS_2)_8$ are ‘moiré metals’ whose undoped and unfolded Fermi wavevectors are much larger than their moiré wavevectors (Supplementary Information). Their Fermiology[13,14] can be tuned through the tunable moiré superlattice of the crystal. Furthermore, our measurements reveal a dense spectrum of quantum oscillation frequencies that are inconsistent with previously proposed non-Onsager mechanisms[12,14]. Instead, this spectrum can be naturally understood by proposing that new oscillation frequencies originate from extremal Fermi-surface orbits that propagate into a synthetic superspace dimension generated by the moiré superlattice, a framework inspired by higher-dimensional superspace models of incommensurate crystallography[15,16]. Our results pave the way towards using bulk moiré materials as superspace crystal platforms for accessing open theoretical proposals in higher dimensions[17–21].

Moiré materials from aperiodic crystals

Our material design principle is depicted in Fig. 1a–c, showing two hypothetical layered compounds (Fig. 1a,b left panels) with hexagonal and monoclinic crystal systems and their in-plane diffraction patterns (Fig. 1a,b right panels). Foliated superlattice materials[31–33] may result from the natural intergrowth of these dissimilar crystals, although not by respecting the competing symmetry constraints of both crystal systems simultaneously. However, an accommodative reaction product that mitigates interlayer lattice frustration could satisfy a partial subset of these symmetry constraints. For example, the schematically depicted rightmost Bragg planes of the hexagonal layers (Fig. 1a middle panel) and monoclinic layers Fig. 1b middle panel) could align to form a new foliated superlattice material (Fig. 1c). Here hexagonal and monoclinic lattices are commensurate along the q_y in-plane lattice direction (*b*-axis) and share a Bragg reflection peak (Fig. 1c right panel). However, this necessarily enforces the two interleaved layer types to be atomically incommensurate along the orthogonal q_x-direction/*a*-axis in the absence of enormous lattice relaxation or reconstruction effects. Hence the result is an aperiodic composite crystal[9–11], accessible through salt-catalysed reactions known to favour foliated superlattice lattice motifs over competing non-superlattice polymorphs[31–33].

Notably, X-ray diffraction techniques such as single-crystal X-ray diffraction (SCXRD) and wide-angle X-ray scattering (WAXS) can identify two distinguishing signatures of aperiodic composite lattices. For $k \gg 0$ (Fig. 1c bottom-left panel), lattice-mismatch incommensurability between adjacent layers appears as a superposition of the diffraction patterns from each layer (Fig. 1c right panel), in which Bragg vectors $\mathbf{G}_1$

and $\mathbf{G}_2$ from different layer types (red and purple spots) are separated by a small wavevector $\mathbf{q} = \mathbf{G}_1 - \mathbf{G}_2$. Near $k = 0$ (Fig. 1c bottom-middle panel), $\mathbf{q}$ itself reveals the modulation of a moiré superlattice derived from the lattice mismatch of the system (distinct from the out-of-plane foliated superlattice). Both signatures are typical of 2D moiré materials[34].

SCXRD measurements (Fig. 1d) of $(Sr_6TaS_8)_{1+\delta}(TaS_2)_8$, a new foliated superlattice material, show Bragg reflections confined to specific q_x (Fig. 1d, arrow markers). Most peaks can be attributed to the hexagonal transition metal dichalcogenide (TMD) monolayers (TaS_2, red circles) or the monoclinic 'spacer' monolayers (Sr_6TaS_8, purple circles). Superimposed peaks from different lattices (concentric circles; $q_y \approx 22$ nm^{-1}) indicate that the TMD and spacer layers share commensurate Bragg planes along the *b*-axis. However, many diffraction peaks cannot be attributed to either lattice individually. Higher-resolution WAXS data show the Bragg reflections of different layers separated by a small momentum $\mathbf{q}$ (Fig. 1f), whereas this same $\mathbf{q}$ and its higher harmonics appear near the origin (Fig. 1e) and as satellites near dominant Bragg reflections (Fig. 1d; Supplementary Information). These features are indicative of a 1D moiré superlattice with a moiré wavelength of $\lambda_m = 2\pi/|\mathbf{q}| \approx 4.13$ nm, comparable with λ_m in 2D moiré heterobilayers[1].

The sharpness of diffraction peaks associated with $\mathbf{q}$ and its influence on scattering extinction conditions (Supplementary Information) demonstrate that naturally grown moiré superlattices show minimal structural disorder throughout the bulk of millimetre-sized crystals. Moreover, nearly identical diffraction patterns obtained from any crystal within a batch (Supplementary Information) evidences the reproducibility and potential scalability of our approach. By contrast, nominally identical device assembly procedures produce 2D moiré superlattices with twist-angle variations and strain gradient profiles[35], highlighting the advantages of our synthesis approach in addressing reproducibility. Given the symmetries of these diffraction patterns (Fig. 1d) and those of related measurements (Supplementary Information), we construct the highest-symmetry model structure consistent with all characterization observables (Fig. 1g). $(Sr_6TaS_8)_{1+\delta}(TaS_2)_8$ manifests our material design principle (Fig. 1a–c), consisting of the natural intergrowth of lattice-mismatched monolayers in a moiré-modulated aperiodic composite structure.

Moiré tunability through material synthesis

An essential feature of moiré materials is their tunability without chemically altering their layers, typically achieved by rotationally misaligning layers manually during the device assembly process[1,2]. We demonstrate that synthesis parameters can offer comparable tunability in bulk moiré materials. Figure 2a–e shows representative crystals from five distinct groups of bulk moiré materials, all ternaries of Sr–Ta–S accessed by means of temperature sequence and precursor stoichiometries variations (Methods). Figure 2b represents the class discussed in Fig. 1d–g. Top-down images show the quasi-1D morphology of these ternary crystals (Fig. 2a–e) with crystal facets that optically differentiate their longer *a*-axis (horizontal) from their shorter *b*-axis (vertical) (Supplementary Information). X-ray diffraction reveals five parent structures, in which the spacer layers 'snap' into q_y-oriented (*b*-axis) commensurate Bragg planes that 3-tuple (a), 5-tuple (b), 8-tuple (c), 11-tuple (d) and 13-tuple (e) the TaS_2 unit cell in this direction. In the orthogonal incommensurate direction (*a*-axis), a wide range of 1D moiré superlattices are realized with various moiré wavelengths λ_m (3.0 to 4.2 nm) and orientation angles φ (±20°) near the *a*-axis. Furthermore, different synthesis conditions produce different moiré superlattices that even share the same commensurate Bragg condition (Supplementary Information). Each structure is denoted STS(n,φ), in which n labels the commensurate Bragg plane order and φ defines the moiré $\mathbf{q}$-vector angle relative to the *b*-axis of the compound.

A natural hypothesis is that crystals grown under different synthesis conditions form chemically distinct ternaries in a complex phase space. However, stoichiometric probes such as wavelength-dispersive X-ray spectroscopy (WDS) rule this out. Across 23 crystal batches, WDS measurements show that the Sr:Ta molar ratios in these compounds are very similar, deviating from the mean by a maximum of 5.1% (most within 3%), comparable with the experimental error of the tool (sulfur stoichiometries were inconclusive; Supplementary Information). This suggests that all of these foliated superlattice materials are the intergrowth of the same two monolayer crystals, TaS_2 and Sr_6TaS_8, with different moiré superlattice structures. To better understand this tunable moiré structure, we conducted high-angle annular dark-field scanning transmission electron microscopy (HAADF-STEM; Fig. 2f) on cross-sectional lamellae of STS(8,81°), for which the diffraction symmetries are more complex than those of STS(5,72°) (Fig. 2b). HAADF-STEM images closely match features of the model structure proposed previously (Fig. 1g) and also visualize the crystal's out-of-plane moiré modulation along the length of these dendritic crystals. Hence HAADF-STEM also suggests that chemically identical TMD and spacer layers intergrow to form a tunable variety of in-plane moiré superlattices.

Given these observations, we propose a comprehensive structural solution that builds bulk moiré crystals modularly from a related commensurate lattice motif[36] (Supplementary Information). This solution is consistent with all characterization data and can naturally explain the five structural families in Fig. 2a–e and many other subtle observations (see Supplementary Information for discussion). Subtle variations in interlayer heterostrain and heteroshear independently change n and φ, stabilizing different STS(n,φ) compounds (Supplementary Information). Furthermore, interlayer heteroshear in bulk moiré materials can be thought of as a continuously tunable analogue to twist angle in 2D moiré materials (Supplementary Information).

Further insights arise from abstracting the TaS_2 and Sr_6TaS_8 lattices as simplified hexagonal and monoclinic lattices (Fig. 2h), respectively, which are strained and sheared according to lattice parameters extracted quantitatively from WAXS (Fig. 2i–k; see Supplementary Information for details). These structures are strictly only atomically incommensurate along their *a*-axis (horizontal); however, Fig. 2j,k mimics strained 2D moiré superlattices in ways that parallel how so-called 'crystalline approximants' mimic quasicrystalline lattices[26]. Whether the electronic properties of these materials are governed by an approximate 2D moiré superlattice or a strictly 1D moiré superlattice remains unresolved at this time and will be investigated in future work.

Quantum oscillations in moiré metals

The electronic properties of moiré materials can be controlled by the structure of their moiré superlattices[1,2], a mechanism that we examine directly through quantum oscillation maps of the Fermiology[13] of bulk moiré metals for fields μ_0H rotated by a polar angle θ within the b–c plane. High-field torque magnetization and magnetotransport measurements (Supplementary Information) reveal a dense cascade of low-frequency oscillations beginning in these moiré compounds near $\mu_0H = 2$ T (Supplementary Information). We first attempt to isolate the influence of the moiré superlattice on Fermiology by comparing quantum oscillations in 'moiré cognate' compounds, STS(8,81°) and STS(8,90°). These compounds are nearly structurally identical (Supplementary Information) but, notably, their moiré $\mathbf{q}$-vectors point in slightly different directions ($\varphi = 81°$ or $90°$) owing to different degrees of interlayer heteroshear established under different growth conditions (Methods).

At high magnetic fields ($\mu_0H > 15$ T), torque magnetization measurements (ΔM_τ; Fig. 3a,b) reveal de Haas–van Alphen oscillations that pull inwards to lower fields $\mu_0H\cos(\theta)$ with increasing θ, suggesting corrugated quasi-2D Fermi pockets (although separate neck and belly frequencies were not identified; see Supplementary Information for more data). Fast Fourier transforms (FFTs) of the temperature-dependent torque magnetization (Fig. 3c,d) of these moiré cognates exhibit

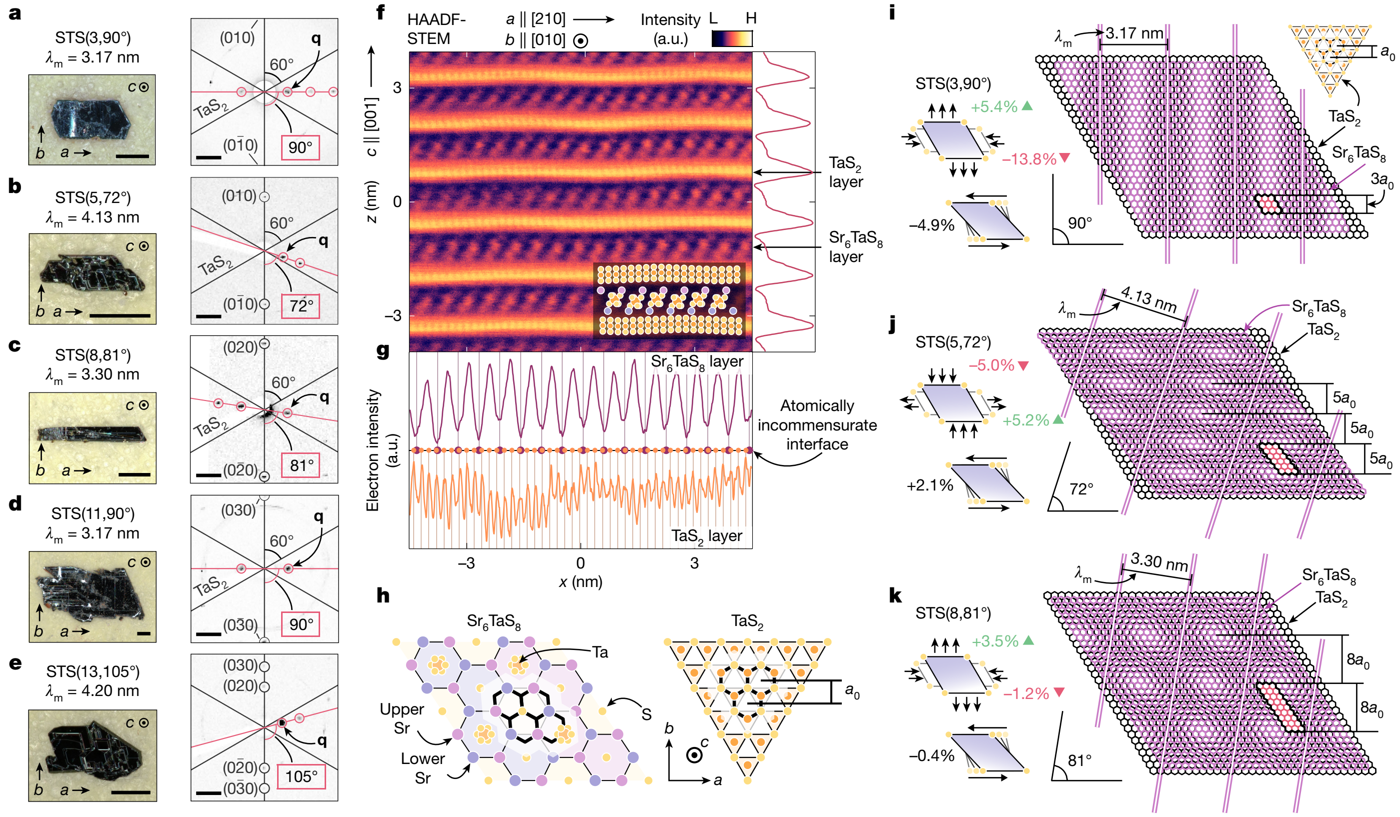

Fig. 2 | Tunable 1D moiré superlattices and 2D moiré approximants. **a**–**e**, Optical images (left panels) and WAXS measurements (right panels) of five related families of bulk moiré materials. The spacer Sr_6TaS_8 layer in each family 'snaps' into q_y-oriented commensurate Bragg planes that 3-tuple (**a**), 5-tuple (**b**), 8-tuple (**c**), 11-tuple (**d**) and 13-tuple (**e**) the TaS_2 unit cell in this direction. Scale bars, 0.2 mm (left panels); 2 nm^{-1} (right panels). **f**, HAADF-STEM cross-sectional image of STS(8,81°) (**c**), which directly visualizes how neighbouring TaS_2 and Sr_6TaS_8 monolayers are mutually incommensurate with each other and are moiré-modulated in the z-direction. **g**, Line cuts of the HAADF-STEM image in **f**. Neighbouring Sr_6TaS_8 and TaS_2 layers are atomically incommensurate with one another. **h**, Simplified visualizations of Sr_6TaS_8 and TaS_2 lattices. **i**–**k**, Large field-of-view, simplified visualizations of representative Sr_6TaS_8/TaS_2 moiré patterns, realized through tunable interlayer couplings between Sr_6TaS_8 and TaS_2 layers. Commensurate Bragg plane conditions (a_0-multiple right labels), the moiré wavelengths λ_m (top labels) and their rotational alignment φ with respect to the TaS_2 lattice (bottom-left labels) are all extracted quantitatively from X-ray diffraction measurements to construct these visualizations. Spacer unit cells are shown by black-outlined red-filled parallelograms. All percentages represent measured deviations of the lattice compression (red numbers), expansion (green numbers) and row-sliding shear (black numbers) of the Sr_6TaS_8 layer lattice relative to an average spacer lattice model. STS(3,90°) represents the simplest structural member of the family with a purely 1D moiré superlattice, whereas STS(5,72°) and STS(8,81°) are representative of structures that are strictly 1D moiré superlattices but similar to 2D moiré approximants owing to further lattice aliasing in the commensurate b-axis. a.u., arbitrary units.

similar amplitude profiles and frequency distributions but they are clearly distinguishable. Notably, by shearing the moiré superlattice from low-symmetry to high-symmetry directions, many neighbouring FFT peaks seem to merge into sharp, isolated ones (Fig. 3c top labels), whereas a few broader peaks split into well-separated ones (Fig. 3d top labels) (see Supplementary Information for a direct comparison). Through Onsager's relation[12], this suggests that the moiré superlattice direction reshapes and resizes Fermi pockets in these bulk crystals. Some of these data can be plausibly explained further by simple Brillouin zone folding arguments (Supplementary Information), but this interpretation neglects several key observations that invite a more careful theoretical treatment.

These discrepancies are particularly apparent in the complex Fermiology of STS(3,90°), the structurally simplest moiré metal studied here. In STS(3,90°), Sr_6TaS_8 and TaS_2 lattices lie in atomic register along the b-axis of the crystal (Fig. 2i), tripling the TaS_2 unit cell along this direction, and a 1D moiré superlattice with $\lambda_m = 3.17$ nm points along the incommensurate a-axis of the crystal. This separates the momentum scales of commensurate and incommensurate Fermi surface reorganization effects and enables us to isolate the salient consequences of a purely 1D moiré superlattice. Figure 4a,b shows the background-subtracted torque magnetization ΔM_τ in two representative crystals up to $\mu_0 H = 31.5$ T. Notably, STS(3,90°) has moderately high-frequency oscillations absent in related compounds (see Supplementary Information for discussion). FFTs of the temperature-dependent torque magnetization (Fig. 4c,d) uncover a rich spectrum of de Haas–van Alphen frequencies. STS(3,90°) also hosts a cascade of low-frequency oscillations, but distinctive combs of FFT peaks extend up to approximately 2,000 T. More than 40 FFT peaks appear at nearly identical frequencies in both samples (black triangle markers; Supplementary Information). These observations are robust under various signal processing windows, especially those that suppress spectral leakage, and to field windowing that includes the high-field regime (see Supplementary Information for full analysis). Using a local-fit peak-finding algorithm (Supplementary Information), we extract the frequencies of FFT peaks, which vary roughly linearly with peak index with an approximate spacing of $\Delta F\cos(\theta) \approx 40$ T (Fig. 4c right inset), a frequency not represented in the ultralow-frequency regime (Fig. 4c,d left insets).

The Fermiology of this simple moiré metal has several seemingly puzzling qualities. First, it seems counterintuitive to find sharp oscillation frequencies in an incommensurate metal without a well-defined Brillouin zone[28]. Furthermore, their peak widths are comparable with those of crystalline metals. Second, the approximate linear frequency

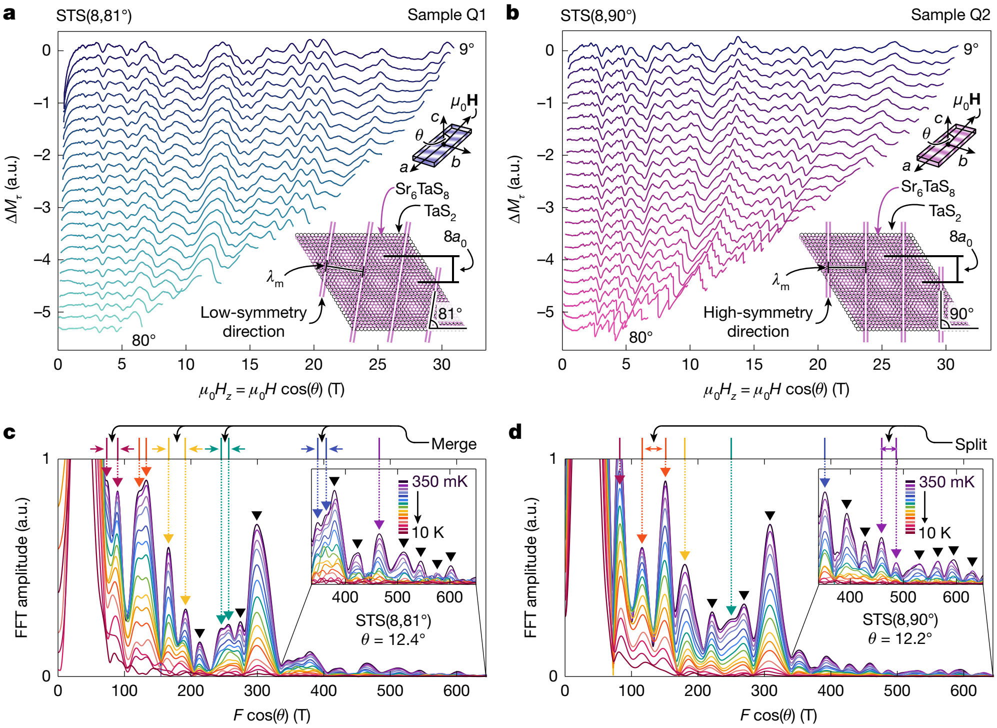

Fig. 3 | Tunable Fermiology in moiré cognate crystals. a, High-field torque magnetization measurements of quantum oscillations in STS(8,81°) for the field μ_0H rotated by a polar angle θ within the b–c plane of the crystal and scaled by the out-of-plane component $\mu_0H\cos(\theta)$. The moiré **q**-vector in STS(8,81°) points along a non-crystallographic, low-symmetry direction, 81° from its b-axis. **b**, Same as **a** but for STS(8,90°), which is related to STS(8,81°) by means of different degrees of interlayer heteroshear. The moiré **q**-vector in STS(8,90°) points along a crystallographic, high-symmetry direction, 90° from its b-axis (that is, along the a-axis). **c**,**d**, FFTs of the temperature-dependent background-subtracted torque magnetization ΔM_τ of STS(8,81°) (**c**) and STS(8,90°) (**d**), showing cascades of low-frequency oscillations. Careful comparisons of these frequencies suggest that nearby Fermi pockets merge with one another (**c**) and split away from one another (**d**) as the layers of these bulk moiré materials shear against one another to sweep the moiré superlattice from a low-symmetry direction (81°) to a high-symmetry direction (90°) with respect to the a-axis. Insets, zoomed-in plots to show further peaks in the FFT with lower FFT amplitudes. a.u., arbitrary units.

spacing of these peaks exhibits a markedly higher degree of order than those of the Fermi surfaces of typical multiband metals, whose Fermi pocket sizes are unrelated to one another. Finally, it is unusual, although not unique, that the extremal areas of these oscillations sum to an area nearly 30-fold larger than the approximate Brillouin zone size for this material (Supplementary Information). There are several non-Onsager mechanisms[12,14] capable of generating new oscillation frequencies unassociated with an extremal Fermi-surface orbit (for example, magnetic breakdown[37,38], quasiparticle lifetime oscillations[39], Weiss oscillations[33,40]). However, these are unlikely for two key reasons. First, the dense comb of frequencies is linearly spaced and spans most of the frequency domain with similar amplitudes. Second, the effective masses of these frequencies increase weakly with peak index, a quantitative feature inconsistent with magnetic breakdown among several other known non-Onsager mechanisms (see Supplementary Information for full discussion).

Moiré metals with superspace dimensions

These initially perplexing observations can be naturally understood by drawing inspiration from a closely related solved problem concerning the crystallography of incommensurate lattices. Before 1960, all solid matter was believed to be either crystalline (Fig. 5a,b) or amorphous[41]. This viewpoint was challenged by discoveries of aperiodic composites[10,11] (Fig. 5c) and quasicrystals[25–27], which exhibit long-range order without periodic unit cells[9]. Without translation symmetry, these lattices cannot support Bloch electronic bands in their physical dimensions (Fig. 5d), although effective theories often suffice[28–30]. Counterintuitively, these crystals exhibit dense arrays of sharp diffraction peaks despite not having a well-defined unit cell[10,11], with peaks widths comparable with those of periodic crystals[26]. This motivated the development of higher-dimensional superspace crystal models[15,16] as a unifying framework for describing incommensurate lattices. In these models, long-range order in incommensurate lattices arises from their description as projections of a higher-dimensional periodic superspace lattice[10] (Fig. 5e). Through this construction, the emergent symmetries of superspace crystals are fully encoded in lower-dimensional incommensurate lattice representations. By comparing our present problem, which aims to explain a dense array of sharp de Haas–van Alphen frequencies in a moiré metal, with this related problem from incommensurate crystallography, we propose that both are similarly rectified by elevating incommensurate structures into emergent superspace dimensions. Such approaches have previously explained static properties of solids, such as atomic lattices and charge densities[10,11], but here we introduce how they apply to dynamic electronic phenomena, such as the Fermi surfaces and cyclotron orbits of itinerant charge carriers.

We propose a momentum-space network model derived from a Lifshitz–Kosevich treatment of quasi-2D metals with incommensurate 1D moiré modulations (see Supplementary Information for details). Its results are intuitively understood as describing quasi-2D Fermi pockets linked at momenta defined by the moiré **q**-vector along an emergent discrete dimension k_ζ (Fig. 5f). This mirrors synthetic dimensions encoded by internal degrees of freedom in recent cold-atom experiments (for example, through hyperfine states)[18,42–44]. In understanding aperiodic composite/moiré lattices in an emergent higher-dimensional space, we regain translation symmetry and therefore regain the ability to describe their properties in terms of Bloch bands of electronic states[45].

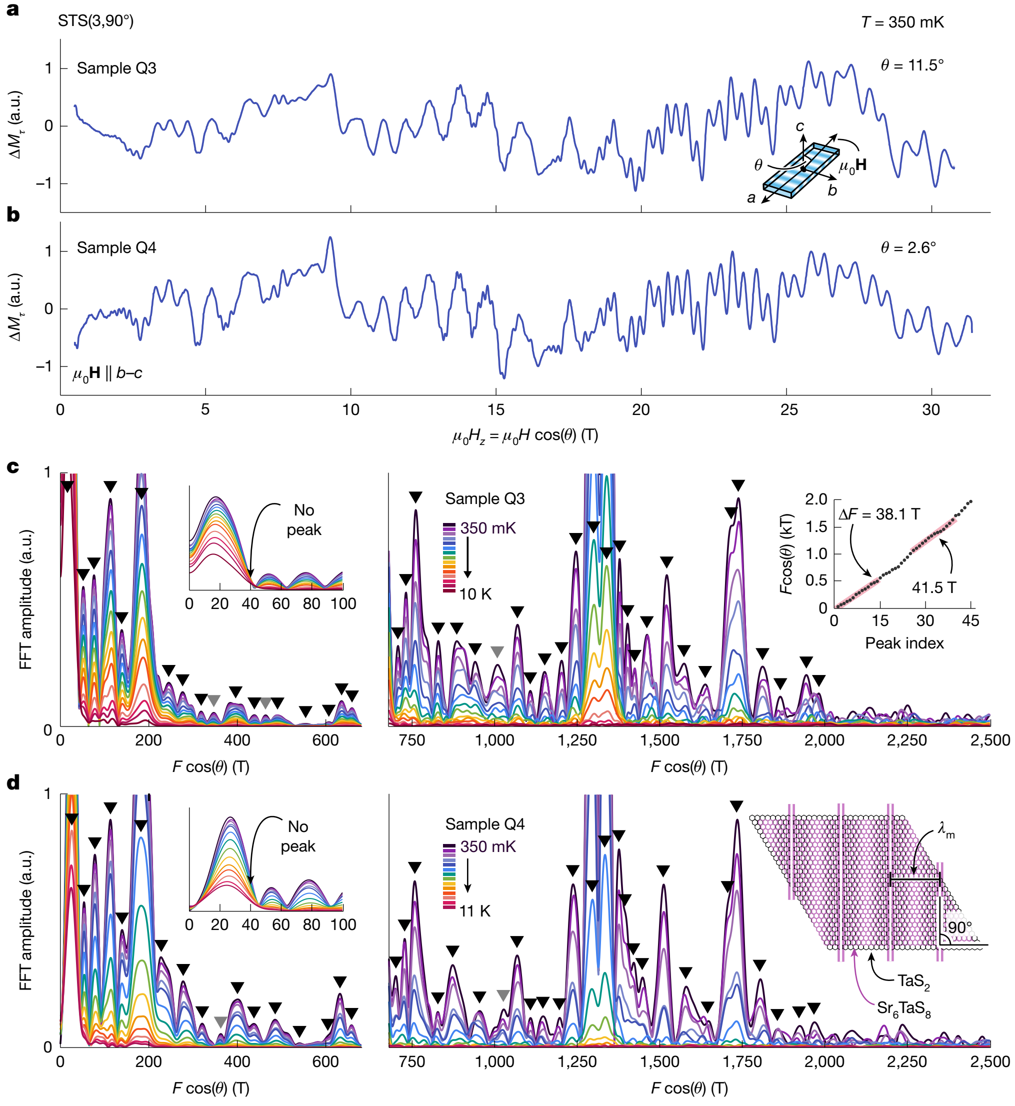

Fig. 4 | de Haas–van Alphen frequency comb in the Fermiology of a simple moiré metal. a,**b**, High-field torque magnetization measurements of quantum oscillations in two crystals of STS(3,90°) for the field $\mu_0 H$ rotated by a polar angle θ within the b–c plane of the crystal and scaled by the out-of-plane component $\mu_0 H\cos(\theta)$. STS(3,90°) is a simple, purely 1D moiré metal with its moiré **q**-vector pointed along its incommensurate a-axis (right inset of **d**). **c**,**d**, FFTs of the temperature-dependent background-subtracted torque magnetization ΔM_τ of each sample of STS(3,90°), showing an abundance of oscillations that are all roughly linearly spaced in frequency. FFT amplitude scaled in the right panels by 12.2× (**c**) and 8× (**d**) for clarity. Black triangle markers identify FFT peaks that are closely shared between datasets. Grey triangle markers identify FFT peaks that are either at slightly different frequencies between datasets or are observed in only one dataset. Left insets, zoomed-in plots of the ultralow-frequency regime of the FFT. Right inset of **c**, extracted FFT peak frequencies as a function of peak index, showing a series of linearly spaced frequencies spaced by roughly $\Delta F\cos(\theta) \approx 40$ T, a value not represented by any observed peak in the low-frequency limit. Fitted peak index regions (red-shaded regions) identify sub-sequences of FFT peaks that appear as clear combs of FFT peaks with relatively similar amplitudes. A linear fit of the entire domain similarly yields linear peak spacings of $\Delta F\cos(\theta) \approx 44.6$ T with $R^2 = 0.996$, a value again not represented by any observed peak in the low-frequency limit. a.u., arbitrary units.

In this picture, a Fermi pocket of the unmodulated structure with cross-sectional area A_k (Fig. 5g) develops into a sequence of fictitious Fermi pockets that increment by discrete areal values A_q for extremal cyclotron orbits that propagate discretely along k_ζ (Fig. 5h). This is distinct from Bragg scattering through the moiré **q**-vector (for example, by magnetic breakdown) and instead is similar to a coherent, local hopping process in a dimension orthogonal to physical space. Ultimately, this proposal explains the complex Fermiology in STS(3,90°), as generated by the ordered extension of the simple three-band Fermi surface of monolayer TaS_2 into a synthetic dimension that generates dense combs of de Haas–van Alphen oscillation frequencies with approximate linear spacing and with comparable FFT amplitudes and effective masses (Fig. 5i,j; see Supplementary Information for further discussion).

So far, most incommensurate metals have exhibited low mobilities, probably because of disorder from more complex formation energetics compared with crystalline materials[27]. Rare exceptions with high mobilities are aptly described by material-specific models that approximate weak incommensurability effects in terms of Bragg scattering and magnetic breakdown[37,38,46,47]. Such models cannot describe the present bulk moiré metals owing to their high mobilities (with mean free paths orders of magnitude larger than λ_m; Supplementary Information) and their pronounced moiré modulations, thus necessitating our generalizable superspace theoretical framework. Also, because of the homogeneity of their moiré **q**-vectors and the sizes of their Fermi pockets, bulk moiré metals act as ideal material platforms for higher-dimensional Fermiology in comparison with 2D moiré semimetals and semiconductors (see Supplementary Information for discussion). Overall, we

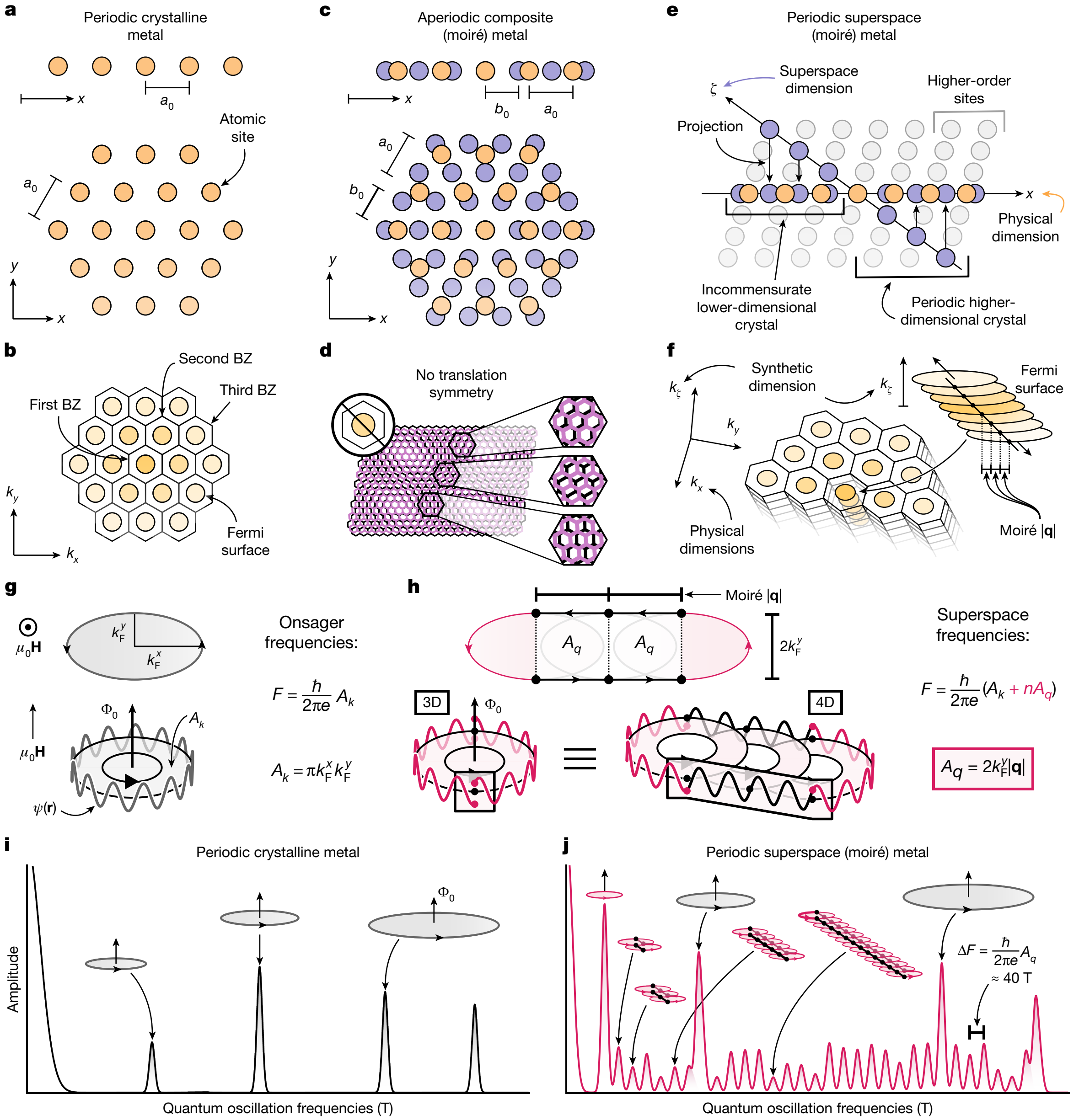

Fig. 5 | Moiré metals as quantum materials with synthetic superspace dimensions. a,**b**, Schematic of the periodic lattice (**a**) and the quasi-2D Fermi surface (**b**) of a quasi-2D crystalline metal. **c**, Schematic of a quasi-2D aperiodic composite/moiré metal lattice. **d**, Schematic of the violated translation symmetry of the aperiodic composite/moiré lattice, which prohibits a complete description of the Fermiology of this metal in 2D. **e**, Schematic of the emergent, higher-dimensional, periodic superspace lattice described by a lower-dimensional aperiodic composite lattice. By elevating the quasi-2D aperiodic lattice into a new superspace dimension ζ, an emergent translation symmetry is restored in (2+1)D. **f**, Schematic of the resulting (2+1)D Fermi surface, making use of the restored translation symmetry. Stacks of quasi-2D Fermi surfaces are linked along a new discrete synthetic dimension k_ζ. **g**, Schematic of an extremal Fermi surface orbit in a crystalline metal, whose associated frequency is given by Onsager's relation. The wavy line depicts the phase of the electronic wavefunction, which is 2π-periodic. **h**, Same as **g** but for a moiré metal. Superspace cyclotron orbits have phase discontinuities in 3D but are continuous and 2π-periodic in 4D. A linear sequence of frequencies originates from superspace Fermi orbits that coherently hop into the synthetic dimension. Real-space orbits rotated by 90° for clarity. **i**,**j**, Schematics of the oscillations frequencies and cyclotron orbits in a quasi-2D crystalline metal (**g**) and a (2+1)D superspace moiré metal (**h**). Cyclotron orbits in the (2+1)D superspace moiré metal propagate by discrete momentum quanta in the synthetic dimension, producing a dense sequence of roughly linearly spaced de Haas–van Alphen oscillations frequencies. BZ, Brillouin zone.

propose that the Fermi surfaces of bulk moiré metals can be understood as (3+1)D Fermi surfaces with three continuous spatial dimensions (k_x, k_y, k_z) and one discrete synthetic dimension (k_ζ).

Discussion

Dimensionality is an idea that is pervasive throughout physics and is often associated with the concept of holography, which captures the relationship between a complete description of a higher-dimensional system that emerges from a lower-dimensional encoded representation. Holography is foundational to many fields of physics, including its use in classical optics to produce projected 3D images from 2D films[48], in holographic dualities to describe the correspondence between gravitational and quantum field theories[49] and in quantum error correction to describe the emergence of fault-tolerant logical qubits from their physical qubits encodings[50]. Similarly, we propose that holography describes the relationship between certain quantum phenomena of higher-dimensional superspace crystals (that is, emergent space) encoded in the lower-dimensional lattice degrees of freedom of tunable aperiodic composite crystals (that is, physical space; see Supplementary Information for discussion). The present work demonstrates how different synthesis conditions can effectively program the aperiodic lattice of bulk moiré materials in ways that encode different superspace crystal lattices. High-resolution quantum oscillation studies evidence the emergent higher-dimensional Fermiology of these superspace crystals and provide a quantitative fingerprint for the incommensurate lattice structure itself.

Looking forward, we predict many directions for realizing physical phenomena that make use of holographic relationships[18,42] (see Supplementary Information for discussion). A rich landscape of theoretical work has predicted higher-dimensional topological phases with exotic bulk–boundary correspondences[19,43,44], as well as unconventional superconductivity that breaks higher-dimensional symmetries[20,21], phenomena traditionally confined to abstract models in four or more spatial dimensions. Broadly, this work demonstrates a powerful new route towards realizing higher-dimensional quantum phases of matter by targeting aperiodic composite materials capable of encoding the requisite emergent superspace lattices for bridging abstract theoretical predictions with experimentally accessible material platforms.

Online content

Any methods, additional references, Nature Portfolio reporting summaries, source data, extended data, supplementary information, acknowledgements, peer review information; details of author contributions and competing interests; and statements of data and code availability are available at https://doi.org/10.1038/s41586-026-10173-8.

1. Mak, K. F. & Shan, J. Semiconductor moiré materials. *Nat. Nanotechnol.* **17**, 686–695 (2022).
2. Nuckolls, K. P. & Yazdani, A. A microscopic perspective on moiré materials. *Nat. Rev. Mater.* **9**, 460–480 (2024).
3. Cao, Y. et al. Unconventional superconductivity in magic-angle graphene superlattices. *Nature* **556**, 43–50 (2018).
4. Cai, J. et al. Signatures of fractional quantum anomalous Hall states in twisted $MoTe_2$. *Nature* **622**, 63–68 (2023).
5. Yasuda, K., Wang, X., Watanabe, K., Taniguchi, T. & Jarillo-Herrero, P. Stacking-engineered ferroelectricity in bilayer boron nitride. *Science* **372**, 1458–1462 (2021).
6. Vizner Stern, M. et al. Interfacial ferroelectricity by van der Waals sliding. *Science* **372**, 1462–1466 (2021).
7. Song, T. et al. Direct visualization of magnetic domains and moiré magnetism in twisted 2D magnets. *Science* **374**, 1140–1144 (2021).
8. Zhao, S. Y. F. et al. Time-reversal symmetry breaking superconductivity between twisted cuprate superconductors. *Science* **382**, 1422–1427 (2023).
9. Cummins, H. Z. Experimental studies of structurally incommensurate crystal phases. *Phys. Rep.* **185**, 211–409 (1990).
10. Smaalen, S. V. *Incommensurate Crystallography* (Oxford Univ. Press, 2007).
11. Janssen, T., Chapuis, G. & de Boissieu, M. *Aperiodic Crystals: From Modulated Phases to Quasicrystals: Structure and Properties* 2nd edn (Oxford Univ. Press, 2018).
12. Onsager, L. Interpretation of the de Haas-van Alphen effect. *Lond. Edinb. Dublin Philos. Mag. J. Sci.* **43**, 1006–1008 (1952).
13. Lifshitz, I. M. & Kosevich, A. M. On the theory of magnetic susceptibility of metals at low temperatures. *Zh. Eksp. Teor. Fiz.* **29**, 730–742 (1955).
14. Leeb, V., Huber, N., Pfleiderer, C., Knolle, J. & Wilde, M. A. A field guide to non-Onsager quantum oscillations in metals. *Adv. Phys. Res.* **4**, 2400134 (2025).
15. de Wolff, P. M. The pseudo-symmetry of modulated crystal structures. *Acta Crystallogr. A* **30**, 777–785 (1974).
16. Janner, A. & Janssen, T. Symmetry of periodically distorted crystals. *Phys. Rev. B* **15**, 643–658 (1977).
17. Hazzard, K. R. A. & Gadway, B. Synthetic dimensions. *Phys. Today* **76**, 62–63 (2023).
18. Ozawa, T. & Price, H. M. Topological quantum matter in synthetic dimensions. *Nat. Rev. Phys.* **1**, 349–357 (2019).
19. Sugawa, S., Salces-Carcoba, F., Perry, A. R., Yue, Y. & Spielman, I. B. Second Chern number of a quantum-simulated non-Abelian Yang monopole. *Science* **360**, 1429–1434 (2018).
20. Sakai, S., Takemori, N., Koga, A. & Arita, R. Superconductivity on a quasiperiodic lattice: extended-to-localized crossover of Cooper pairs. *Phys. Rev. B* **95**, 024509 (2017).
21. Cao, Y. et al. Kohn-Luttinger mechanism driven exotic topological superconductivity on the Penrose lattice. *Phys. Rev. Lett.* **125**, 017002 (2020).
22. Evans, H. T. & Allmann, R. The crystal structure and crystal chemistry of valleriite. *Z. Kristallogr. Cryst. Mater.* **127**, 73–93 (1968).
23. Yadav, A. K. et al. Observation of polar vortices in oxide superlattices. *Nature* **530**, 198–201 (2016).
24. Wiegers, G. A. Misfit layer compounds: structures and physical properties. *Prog. Solid State Chem.* **24**, 1–139 (1996).
25. Shechtman, D., Blech, I., Gratias, D. & Cahn, J. W. Metallic phase with long-range orientational order and no translational symmetry. *Phys. Rev. Lett.* **53**, 1951–1953 (1984).
26. Goldman, A. I. & Kelton, R. F. Quasicrystals and crystalline approximants. *Rev. Mod. Phys.* **65**, 213–230 (1993).
27. Bancel, P. A., Heiney, P. A., Stephens, P. W., Goldman, A. I. & Horn, P. M. Structure of rapidly quenched Al-Mn. *Phys. Rev. Lett.* **54**, 2422–2425 (1985).
28. Zhang, Y., Maharaj, A. V. & Kivelson, S. Disruption of quantum oscillations by an incommensurate charge density wave. *Phys. Rev. B* **91**, 085105 (2015).
29. Suárez Morell, E., Correa, J. D., Vargas, P., Pacheco, M. & Barticevic, Z. Flat bands in slightly twisted bilayer graphene: tight-binding calculations. *Phys. Rev. B* **82**, 121407 (2010).
30. Bistritzer, R. & MacDonald, A. H. Moiré bands in twisted double-layer graphene. *Proc. Natl Acad. Sci.* **108**, 12233–12237 (2011).
31. Devarakonda, A. et al. Clean 2D superconductivity in a bulk van der Waals superlattice. *Science* **370**, 231–236 (2020).
32. Ma, K. et al. Two-dimensional superconductivity in a bulk superlattice van der Waals material $Ba_6Nb_{11}Se_{28}$. *Phys. Rev. Mater.* **6**, 044806 (2022).
33. Devarakonda, A. et al. Evidence of striped electronic phases in a structurally modulated superlattice. *Nature* **631**, 526–530 (2024).
34. Yoo, H. et al. Atomic and electronic reconstruction at the van der Waals interface in twisted bilayer graphene. *Nat. Mater.* **18**, 448–453 (2019).
35. Lau, C. N., Bockrath, M. W., Mak, K. F. & Zhang, F. Reproducibility in the fabrication and physics of moiré materials. *Nature* **602**, 41–50 (2022).
36. Khasanova, N. R. et al. A new structure type of the ternary sulfide $Eu_{1.3}Nb_{1.9}S_5$. *J. Solid State Chem.* **164**, 345–353 (2002).
37. Everson, M. P., Johnson, A., Lu, H.-A., Coleman, R. V. & Falicov, L. M. Magnetoquantum oscillations, magnetic breakdown, and Fermi-surface modifications in $NbSe_3$. *Phys. Rev. B.* **36**, 6953–6962 (1987).
38. Hill, S. et al. Quantum limit and anomalous field-induced insulating behavior in η-Mo_4O_{11}. *Phys. Rev. B.* **55**, 2018–2031 (1997).
39. Huber, N. et al. Quantum oscillations of the quasiparticle lifetime in a metal. *Nature* **621**, 276–281 (2023).
40. Gerhardts, R. R., Weiss, D. & Klitzing, K. V. Novel magnetoresistance oscillations in a periodically modulated two-dimensional electron gas. *Phys. Rev. Lett.* **62**, 1173–1176 (1989).
41. Janssen, T. Aperiodic crystals: a contradictio in terminis? *Phys. Rep.* **168**, 55–113 (1988).
42. Boada, O., Celi, A., Latorre, J. I. & Lewenstein, M. Quantum simulation of an extra dimension. *Phys. Rev. Lett.* **108**, 133001 (2012).
43. Lohse, M., Schweizer, C., Price, H. M., Zilberberg, O. & Bloch, I. Exploring 4D quantum Hall physics with a 2D topological charge pump. *Nature* **553**, 55–58 (2018).
44. Zilberberg, O. et al. Photonic topological boundary pumping as a probe of 4D quantum Hall physics. *Nature* **553**, 59–62 (2018).
45. Lu, J. P. & Birman, J. L. Electronic structure of a quasiperiodic system. *Phys. Rev. B.* **36**, 4471–4474 (1987).
46. Batalla, E., Razavi, F. S. & Datars, W. R. Fermi surface of $Hg_{3-\delta}AsF_6$ and $Hg_{3-\delta}SbF_6$. *Phys. Rev. B.* **25**, 2109–2118 (1982).
47. Kawamoto, T. et al. Fermi surface of the organic superconductor $(MDT\text{–}ST)(I_3)_{0.417}$ reconstructed by incommensurate potential. *Phys. Rev. B* **73**, 024503 (2006).
48. Schnars, U. & Jüptner, W. Direct recording of holograms by a CCD target and numerical reconstruction. *Appl. Opt.* **33**, 179–181 (1994).
49. Bousso, R. The holographic principle. *Rev. Mod. Phys.* **74**, 825–874 (2002).
50. Pastawski, F., Yoshida, B., Harlow, D. & Preskill, J. Holographic quantum error-correcting codes: toy models for the bulk/boundary correspondence. *J. High Energy Phys.* **2015**, 149 (2015).

Methods

Single-crystal synthesis

For full details of each growth recipe, see the Supplementary Information. Briefly, SrS powder, Ta powder, S pieces and either $SrBr_2$ powder (for only STS(3,90°)) or $SrCl_2$ beads (for all other compounds) were combined in an Ar glovebox and placed into an alumina crucible, which was inserted into a quartz tube. This ampoule was sealed at approximately 5×10^{-7} Torr without air exposure and grown under different temperature sequences for each moiré superlattice, as detailed fully in the Supplementary Information. In total, the moiré superlattices in STS(n,φ) compounds are controlled by the growth's precursor stoichiometry (SrS:Ta:S), its temperature sequence and its salt catalyst ($SrBr_2$ or $SrCl_2$).

X-ray diffraction

WAXS measurements were performed using the facilities of MIT.nano. Thin (<100 µm) plate-like crystals were affixed to etched SiN_x windows using silicone vacuum grease. Samples were analysed using a SAXSLAB Retro-F instrument at room temperature under X-ray irradiation directed along the out-of-plane c-axis of the crystal. SCXRD measurements were performed in the MIT Chemistry Department X-Ray Diffraction Facility. Crystals were mounted on a MiTeGen loop using paratone oil. Samples were cooled to 100 K using liquid nitrogen and analysed using a Bruker Single Crystal X-Ray Diffractometer.

Wavelength-dispersive X-ray spectroscopy

WDS measurements were performed in the MIT Electron Microprobe Facility. Flat-plate-like single-crystal samples were chosen of each compound and affixed to a glass slide using carbon tape. This glass slide was then coated with a thin conductive film to eliminate charging artefacts and the samples were analysed using a JEOL JXAS-8200 Superprobe capable of performing scanning electron microscopy imaging and wavelength-dispersive spectroscopy measurements of the stoichiometries of crystals. Before each session of stoichiometric measurements performed on all of the single crystals affixed to a single glass slide, the tool was calibrated against a set of standard samples with known stoichiometric ratios of Sr, Ta, S, O and Cl.

Torque magnetometry

Torque magnetometry measurements were performed at Cell 9 (main text) and Cell 6 (Supplementary Information) of the National High Magnetic Field Laboratory and in a commercial 14-T in-house cryostat (Supplementary Information). Torque was measured using piezoresistive cantilevers (SCL Sensor.Tech PRSA-L300) with an excitation amplitude of 25 mV applied to the top and bottom nodes of a resistive bridge including the sample piezoresistive cantilever and a room-temperature variable resistor used for balancing the bridge. de Haas–van Alphen oscillations of the torque magnetization were analysed after a smooth polynomial background (often quadratic or quartic) was removed from the raw torque signal and the background-subtracted signal was Fourier transformed with the use of a Blackman windowing function to suppress spectral leakage artefacts. Details of this analysis and the role of the field window, the windowing function and the background subtraction in the analyses are discussed in the Supplementary Information.

Magnetotransport measurements

Longitudinal transport measurements were performed at Cell 6 of the National High Magnetic Field Laboratory. Current excitation of 1–2 mA was applied along the a-axis of the crystal and voltage modulations were detected using the standard a.c. technique with a lock-in amplifier.

Theoretical calculations and modelling

For full details about the momentum-space network model derived from a Lifshitz–Kosevich treatment of quasi-2D metals with incommensurate 1D moiré modulations, see the Supplementary Information.

Data availability

The data that support the findings of this study are available from the corresponding author on reasonable request.

Acknowledgements We thank S. Y. F. Zhao, P. Neves, A. Mayo, E. S. Choi, P. Müller, J. Oppenheim, N. Chatterjee, H. Rezeau, J. Cox and C. Settens for their technical support of this project and for useful discussions. We thank the MIT Chemistry Department X-Ray Diffraction Facility, the MIT Electron Microprobe Facility and the National High Magnetic Field Laboratory for making this work possible. This work was financed, in part, by the Gordon and Betty Moore Foundation EPiQS Initiative, grant no. GBMF9070 (synthesis instrumentation and computation), the U.S. Department of Energy (DOE) Office of Science, Basic Energy Sciences, under award DE-SC0022028 (material development), the Office of Naval Research (ONR) under award N000142412407 (material analysis) and ARO grant no. W911NF-24-1-0234 (measurement technique development) to J.G.C. K.P.N. acknowledges support from the MIT Pappalardo Fellowship in Physics. Support for the theory–experimental collaboration reported here was provided by the Air Force Office of Scientific Research (AFOSR), under award FA9550-22-1-0432 to L.F. and J.G.C. F.G. is grateful for the financial support from the Swiss National Science Foundation (Postdoc.Mobility grant no. 222230). Part of this work was performed at the National High Magnetic Field Laboratory, which is supported by the National Science Foundation Cooperative Agreement No. DMR-2128556 and the State of Florida. This work was also carried out in part through the use of MIT.nano's facilities. The imaging work was supported by the STC Center for Integrated Quantum Materials, NSF grant no. DMR-1231319 and it was performed in part at the Harvard University Center for Nanoscale Systems (CNS), a member of the National Nanotechnology Coordinated Infrastructure Network (NNCI), which is supported by the National Science Foundation under NSF award no. ECCS-2025158.

Author contributions K.P.N. and J.G.C. designed the experiments. K.P.N. discovered the compounds used for the study, with input on their synthesis from T.S. and J.G.C. K.P.N. performed structural characterization of the compounds and fabricated torque magnetometry and magnetotransport samples used in measurements. K.P.N. performed torque magnetometry and magnetotransport measurements, with measurement support from A.C. and J.P.W. and with technical support from D.G. High-angle annular dark-field scanning transmission electron microscopy measurements were performed by A.A., with support from J.G., A.J.A. and D.C.B. Theoretical modelling and calculations were performed by N.P. and F.G., with guidance from L.F. and with input from K.P.N., A.C. and J.G.C. All authors discussed the results and contributed to the writing of the manuscript.

Competing interests The authors declare no competing interests.

Additional information
Supplementary information The online version contains supplementary material available at https://doi.org/10.1038/s41586-026-10173-8.
Correspondence and requests for materials should be addressed to Joseph G. Checkelsky.
Peer review information *Nature* thanks Vladimir Fal'ko and the other, anonymous, reviewer(s) for their contribution to the peer review of this work. Peer reviewer reports are available.
Reprints and permissions information is available at http://www.nature.com/reprints.